Electrochimica Acta 265 (2018) 10–18

Contents lists available at ScienceDirect

Electrochimica Acta

journal homepage: www.elsevier.com/locate/electacta

The role of Cr doping in Ni–Fe oxide/(oxy)hydroxide electrocatalysts for oxygen evolution

Dongyu Xu [a, b], Michaela Burke Stevens [b], Yichuan Rui [c], Giovanni DeLuca [d, e, f], Shannon W. Boettcher [b], Elsa Reichmanis [d, e, f], Yaogang Li [g], Qinghong Zhang [a, g, *], Hongzhi Wang [a, **]

[a] State Key Laboratory for Modification of Chemical Fibers and Polymer Materials, College of Materials Science and Engineering, Donghua University, Shanghai, 201620, People's Republic of China
[b] Department of Chemistry and Biochemistry, University of Oregon, Eugene, OR 97403, United States
[c] College of Chemistry and Chemical Engineering, Shanghai University of Engineering Science, Shanghai, 201620, People's Republic of China
[d] School of Chemistry and Biochemistry, Georgia Institute of Technology, 901 Atlantic Drive, Atlanta, GA, 30332, United States
[e] School of Chemical and Biomolecular Engineering, Georgia Institute of Technology, 311 Ferst Drive NW, Atlanta, GA, 30332, United States
[f] School of Material Science and Engineering, Georgia Institute of Technology, 771 Ferst Drive NW, Atlanta, GA, 30332, United States
[g] Engineering Research Center of Advanced Glasses Manufacturing Technology, MOE, Donghua University, Shanghai, 201620, People's Republic of China

ARTICLE INFO

Article history:
Received 27 October 2017
Received in revised form
28 December 2017
Accepted 23 January 2018

Keywords:
Oxygen evolution
Electrocatalysts
Nickel iron oxides
Chromium
Electrochemical impedance

ABSTRACT

Efficient and earth-abundant electrocatalysts for water oxidation are essential for renewable and sustainable energy conversion technologies. And Ni(Fe)O_xH_y especially attractive as a state-of-the-art best candidate catalyst for efficient electrochemical oxygen evolution reaction (OER). In previous research, Cr has been reported could benefit the Ni(Fe)O_xH_y catalysts with conflicting mechanism. Here, a series of ternary (Ni, Fe and Cr) amorphous metal oxide catalysts for OER are synthesized via a simple thermal decomposition method. We show that $Ni_{0.6}Fe_{0.3}Cr_{0.1}O_x$ has a turnover frequency of $0.046 \pm 0.004\ s^{-1}$ at 300 mV overpotential which is ~31% more active than an analogous $Ni_{0.6}Fe_{0.4}O_x$ film, $0.035 \pm 0.007\ s^{-1}$, in 0.1 M KOH media. Using electrochemical voltammetry and AC impedance analysis, we demonstrate that Cr increases the number of electrochemically available active sites, as a pore forming agent, but does not affect the intrinsic per metal atom activity. We find that the Cr begins to leach immediately upon electrochemical testing, and the Cr is almost completely depleted after a 24 h stability test. Importantly, along with the decreased content of Cr, the catalyst activity is further promoted. Although the Cr itself may not be responsible for the improvement, its dissolution results in an ideal type of pore and/or active sites. We further optimize the deposition of high-surface-area and high-mass-loading $Ni_{0.6}Fe_{0.3}Cr_{0.1}O_x$ on carbon-cloth electrodes and demonstrate an overpotential as low as 251 mV at 10 mA cm^{-2} in 1 M KOH.

1. Introduction

Hydrogen can be generated renewably with solar energy through photoelectrochemical water splitting or by water electrolysis. Water splitting reactions can be divided into two half-reactions: the hydrogen evolution reaction (HER) and the oxygen evolution reaction (OER) [1]. The slow kinetics of the four-electron transfer process and the O=O double bond formation during the OER limits the overall performance of water splitting [2]. Multi-component metal oxides/(oxy)hydroxides containing Ni, Co, Fe, and Mn are the promising candidates for the high-efficiency and low-cost OER electrocatalysts [3–6]. Fundamentally understanding the function and effect of each element in these earth-abundant catalysts is essential for the development of electrocatalysts with improved activities.

Among earth-abundant OER catalysts studied, Ni–Fe oxides/(oxy)hydroxides are among the most active catalysts in basic electrolyte [3,6–9]. Historically, Ni oxide/(oxy)hydroxides have been considered very active catalyst materials [10,11]. However, Corrigan and Trotochaud et al. have demonstrated that Ni (oxy) hydroxides are actually poor catalysts and that co-deposition or

* Corresponding author. State Key Laboratory for Modification of Chemical Fibers and Polymer Materials, College of Materials Science and Engineering, Donghua University, Shanghai, 201620, People's Republic of China.
** Corresponding author.
E-mail addresses: zhangqh@dhu.edu.cn (Q. Zhang), wanghz@dhu.edu.cn (H. Wang).

https://doi.org/10.1016/j.electacta.2018.01.143
0013-4686/

unintentional contamination (high purity electrolyte, etc) of Fe increases the activity of Ni (oxy)hydroxides by three orders of magnitudes compared to the pure Ni (oxy)hydroxides in rigorously Fe-free conditions [9,12]. The role of Fe in these Ni(Fe) (oxy)hydroxides is still debated, however, Fe is clearly a critical component for high activity [9,13–15].

Previous research shows that the introduction of a third metal could further improve the OER activity in Ni–Fe oxides/(oxy)hydroxides. Smith et al. proposed a synergistic effect among ternary Ni, Co, and Fe (oxy)hydroxides through a photochemical route [16]. Zhang et al. found that the addition of Al into Ni–Fe could benefit the OER catalysts, and correlated the promoted activity to the high Lewis-acidity of Al^{3+} facilitating the concerted M-O bond formation and deprotonation [17]. It has been previously reported that incorporation of a certain amounts of Cr could promote the OER activity of Ni–Fe oxides/hydroxides [18–21]. Singh et al. synthesized a series of spinel-type $NiFe_{2-x}Cr_xO_4$ oxides by the precipitation method, and the best electrocatalytic activity of the oxide was achieved with $x = 0.8–1.0$ [18]. Diaz-Morales et al. demonstrated that NiCr LDH (with Fe impurities) had superior activity than Ni(Fe) hydroxides by a joint theoretical-experimental study, and doping with Cr could lower the overpotential through tuning adsorption energies of *O and *OH [21]. In a separate investigation, Lange and coworkers correlated OER activity of annealed $Ni_{1-y-z}Fe_yCr_zO_x$ with electronic/physical structure and suggested that the OER activity benefited from the addition of Cr due to an increased ratio of octahedral Fe^{III} to tetrahedral Fe^{III} [19]. Stahl and coworkers also observed that the NiFe oxide OER activity was enhanced with Cr-doping and they attributed the improved activity to the interactions between these redox-active ions and Lewis-acidity of the Cr cations [20]. In addition to the conflicting role of Cr, the stability of Cr in NiFeCr oxide/(oxy)hydroxide catalysts is unclear [18,19,21].

The role of crystallinity has also been thoroughly studied and highly crystalline and rigid electrocatalysts generally underperform more-disordered so-called “amorphous” catalyst films [16,22]. This is likely because the active phases in many cases are (oxy)hydroxides under OER conditions regardless of the initial as-synthesized structure [3]. Amorphous oxides appear easier to convert to active (oxy)hydroxides phases than highly crystalline oxide catalysts [3,23–26]. Here we investigate a series of amorphous ternary metal oxides containing well-defined compositions (Ni, Fe, and Cr) prepared by a thermal decomposition method. The overpotentials of the ternary metal catalysts for water oxidation are mapped as a function of composition. The role of Cr in activity and long-term stability was tested via cyclic voltammetry and polarization. X-ray photoelectron spectroscopy (XPS) and inductively coupled plasma optical emission spectrometry (ICP-OES) were used to monitor the surface and bulk compositions. We find that Cr leaches from the catalyst system during the course of the water oxidation process, which increases the performance of the Ni–Fe oxides/(oxy)hydroxides electrocatalyst by increasing the number of electrochemically available active sites. This indicates that Cr itself is unrelated with the high performance OER catalysts outside of its role as a pore-forming agent. The elucidation of the working mechanism of Cr content provides insight that will enable understanding the function of other thermodynamically unstable elements in multicomponent catalysts and designing effective porous/disordered electrocatalysts for water oxidation.

2. Experimental

2.1. Synthesis of amorphous films on planar substrates

Precursor solutions were prepared from nickel (II) 2-ethylhexanoate (78% w/w in 2-ethylhexanoic acid, Strem Chemicals), iron (III) 2-ethylhexanoate (50% w/w in mineral spirits, Strem Chemicals) and chromium (III) 2-ethylhexanoate (50% w/w in 2-ethylhexanoic acid, Alfa Aesar). Amorphous metal oxide films were prepared on fluorine-doped tin oxide (FTO) coated glass substrates (TEC-15, Pilkington) or Au/Ti through a modified near-infrared-driven (NIR) decomposition of metal-complex method (Scheme 1a) [27]. First, the solutions were prepared by dissolving the precursors in hexane to produce the total metal-complex concentration of 15 wt%. The mixed precursors were sonicated for 10 min to achieve homogeneous mixing. Then the solutions were spin-coated on FTO at 3000 rpm for 45 s. Second, the films were placed under a near-infrared lamp (Philips BR125 IR 150 W) with different irradiation time, where the bottom of the lamp was positioned 2 cm above the substrate that was set on an Al_2O_3 ceramic wafer to dissipate the heat. The temperature of substrate is about 220 °C, determined by a thermocouple.

2.2. Construction of catalysts/carbon cloth electrode

The electrocatalyst was loaded on carbon cloth (CC) by an impregnation method (Scheme 1b). The CC was dipped in the precursor solution for 5 s. Then the sample was treated with the NIR lamp irradiation (by the above-mentioned preparation method).

2.3. Electrochemical characterization

As-prepared electrodes were masked with a 60 μm Surlyn film (Solaronix) with a 0.25 cm^2 square hole to explore the active areas. Surlyn films were adhered to the electrodes after heating to 115 °C. The electrochemical measurements were performed using Zennium workstation (Zarhner, Inc.) or BioLogic SP200/SP300 in a home-built three-electrode electrochemical system in 0.1 M KOH electrolyte (Semiconductor grade, Sigma-Aldrich, without further purification). High-purity oxygen was bubbled through the electrolyte 20 min before and during the electrochemical test. A platinum wire and standard Hg/HgO were employed as a counter electrode (CE) and reference electrode (RE), respectively. The potential of the Hg/HgO reference electrode (*vs*. RHE) was calibrated against a reversible hydrogen electrode.

All potentials reported here were normalized to the overpotential (according to Equation (1)). The cyclic voltammetry for the integration of the Ni redox wave was performed with a scan rate of 10 mV s^{-1}. The onset-potential ($J = 0.1$ mA cm^{-2}), stable catalytic potential ($J = 1$ mA cm^{-2}) and Tafel slopes were measured by the galvanostatic method. Electrochemical impedance spectroscopy (EIS) was measured in the 0.1 M KOH solution with an amplitude of 5 mV and frequencies between 0.1 Hz and 1 MHz at a potential of 0.6 V *vs* Hg/HgO. The electrochemical measurements were corrected for R_u, the uncompensated series resistance. R_u was determined by equating R_u to the minimum impedance between 1 kHz and 1 MHz, where the phase angle was closest to zero. Typically, for the catalyst on FTO electrodes in 0.1 M KOH, R_u was ~30–50 Ω.

$$\eta = \boldsymbol{E}_{\text{measured}} - \boldsymbol{E}_{\text{rev}} - \boldsymbol{iR}_u \text{ with } \boldsymbol{E}_{\text{rev}} = 0.30 \text{ V at } 25\,^{\circ}\text{C} \quad (1)$$

The average total turnover frequency (TOF), i.e. the number of O_2 formed per s per metal ion, is calculated based on the number total metal atoms (including Ni, Fe and Cr) and the steady-state current at 300 mV iR-compensated overpotential according Equation (2). The number of total metal is measured by ICP-OES from the dissolved sample following electrochemical analysis.

$$\mathrm{TOF} = \frac{\frac{Current\ (A)\ \ at\ \eta{=}300\ mV}{96485\left(\frac{C}{mol}\right)\times 4}}{Number\ of\ total\ metal\ (mol)} \quad (2)$$

2.4. Materials characterization

Film morphology was analyzed by a field emission scanning electron microscope (FE-SEM, Hitachi S-4800) and atomic force microscopy (AFM, Bruker Dimension Icon). The decomposition of the metal-complex was tracked by Fourier transform infrared spectroscopy (FTIR, Nicolet 6700 with ATR attachment). Transmission electron microscope (TEM, JEOL-2010) operated at 200 kV was used to study crystallization. X-ray diffraction (XRD) analysis was carried out on a Rigaku D/max-2550 PC using Cu Kα radiation. X-ray photoelectron spectroscopy (XPS) measurements were carried out on a Kratos Axis Ultra DLD X-ray photoelectron spectrometer using a source of Al Kα radiation with energy of 1486.6 eV. The catalyst film was dissolved by concentrated HNO_3, and then diluted with nanopure water. The concentration of solution was tested with ICP-OES (Optima 2100 DV, PerkinElmer) to calculate the mass loading.

3. Results and discussion

3.1. Catalyst preparation and characterization

The amorphous ternary oxide films with different stoichiometric ratios were synthesized by a modified NIR-driven decomposition method. The precursor solution was spin-coated onto FTO and the film was set under an infrared lamp for 2 h in air. The mass loading of the catalyst on planar substrates (FTO and Au/Ti) was about 40–50 μg cm^{-2} as determined by ICP-OES. As presented in Fig. S1, the as-prepared $Ni_{0.6}Fe_{0.4}O_x$ (Fig. S1a) and $Ni_{0.6}Fe_{0.3}Cr_{0.1}O_x$ (Fig. S1b) films were shown to be smooth, featureless, and defect free using FE-SEM imaging. As seen by AFM, the root-mean-square surface roughness (R_{rms}) of the amorphous films is near 0.3 nm (Fig. S2). During the thermal decomposition process, the metal ligands decomposed to the metal oxide, characterized by FTIR (Fig. S3a). The thickness of each sample is about 100 nm, confirmed by FE-SEM cross-sectional images (Fig. S4). With an increase in radiation time, the intensity of the C–H and C–O stretching vibration bands decreased, indicating the liberation of the ligands. Table S1 provides a detailed ICP-OES and XPS analysis to assess the atomic ratio for each sample, the results of which confirm that stoichiometry was controlled accurately.

Catalyst crystallinity was investigated by TEM and XRD. TEM images of $Ni_{0.6}Fe_{0.4}O_x$ and $Ni_{0.6}Fe_{0.3}Cr_{0.1}O_x$ (Fig. 1) whereby the catalysts were scratched off the FTO substrates are provided, which show the absence of lattice fringes and Debye rings, illustrating the amorphous nature of both catalysts. The as-synthesized film was further characterized by XRD (Fig. S5) and, with the exception of the diffraction peak associated with SnO_2 (JSPDS: 40–1088) from FTO, no obvious crystallization peaks were observed. These analyses indicate that the as-synthesized catalysts are amorphous, which strongly suggests that they are likely to have local structures consistent with small grain (oxy)hydroxide phases at OER relevant potentials.

3.2. Electrochemical properties

The electrochemical water oxidation performance of the ternary metal oxide catalysts was investigated by polarization in 0.1 M KOH electrolyte with iR-compensation. Before evaluating the OER performance, the catalysts were activated using cyclic voltammetry (Fig. S6). The OER activity of catalysts on FTO substrate reaches stable OER performance after 20 cycles with scan rate of 10 mV s^{-1}. Through the activation process, the growth of redox peaks and OER current was observed, indicating an increase in ion-permeability. This is likely due to the *in situ* transformation of amorphous oxide to the layered (oxy)hydroxide [3]. Except the specific description, all the electrochemical measurement in this manuscript are performed after 20 cycles activation. Two parameters were selected as benchmarks for water oxidation kinetics: (i) onset overpotential (η, when $J = 0.1$ mA cm^{-2}), and (ii) overpotential (η, when $J = 1$ mA cm^{-2}). Owing to overlap between the Ni oxidation peak and OER current, we used chronopotentiometry to measure overpotentials for catalyst comparison instead of CVs. Although these benchmarking parameters do not give the intrinsic activity, they do allow for a comparison of catalyst performance, as the catalyst films were prepared from identical synthesis processes and the loading mass of each sample is similar. The sensitivity of catalytic performance to the elemental composition is mapped in Fig. 2.

Examination of Fig. 2 reveals that, consistent with previous research, several Ni-rich and Ni–Fe binary oxides have a high performance with a low onset potential [16,17]. Upon addition of Cr, the onset-potential initially decreases, however, when the Cr composition approaches and exceeds 50%, catalyst performance declines substantially and CrO_x is inactive for the OER. Among these compositions, the best catalytic performance was achieved for $Ni_{0.6}Fe_{0.3}Cr_{0.1}O_x$, which exhibited an onset potential of 232 ± 2 mV vs. 241 ± 2 mV (at 0.1 mA cm^{-2}) for the Cr-free $Ni_{0.6}Fe_{0.4}O_x$ derivative with the same loading mass (~ 45 μg cm^{-2}). Note that, the onset potential and stable water oxidation potential display the similar

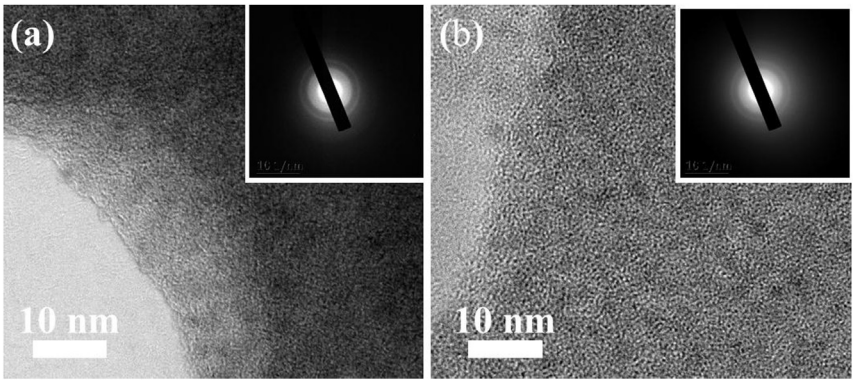

Fig. 1. High resolution TEM images of $Ni_{0.6}Fe_{0.4}O_x$ (a) and $Ni_{0.6}Fe_{0.3}Cr_{0.1}O_x$ (b). The corresponding selected area electron diffraction patterns are provided in the inserts.

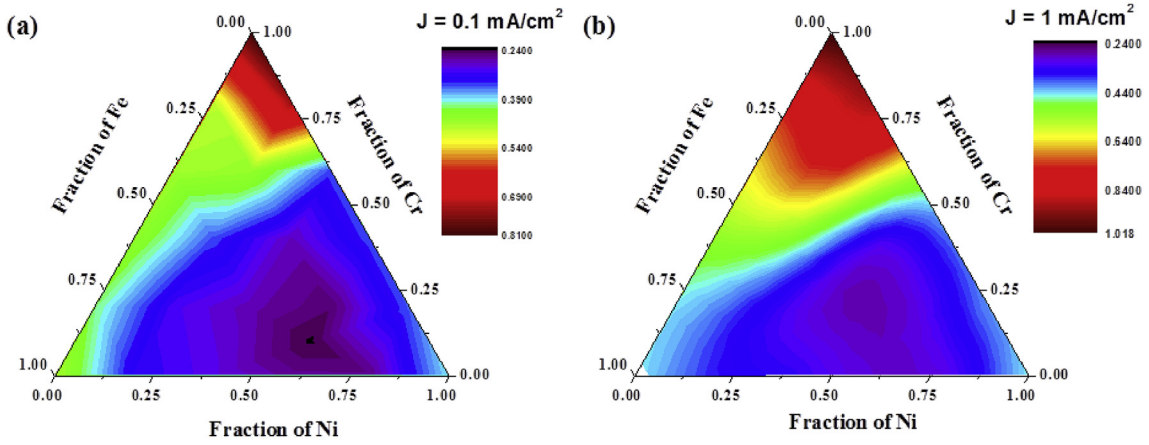

Fig. 2. Contour plots of kinetic parameters of amorphous (mixed) metal oxide films on FTO substrates: (a) onset potential (η, $J = 0.1\ mA\ cm^{-2}$) and (b) stable catalytic potential (η, $J = 1\ mA\ cm^{-2}$).

trend. Both of $Ni_{0.6}Fe_{0.4}O_x$ and $Ni_{0.6}Fe_{0.3}Cr_{0.1}O_x$ catalysts show excellent water oxidation performance, $\eta = 285 \pm 2$ mV for the $Ni_{0.6}Fe_{0.4}O_x$ and the $\eta = 273 \pm 3$ mV for the $Ni_{0.6}Fe_{0.3}Cr_{0.1}O_x$ at $1\ mA\ cm^{-2}$. The activity of $Ni_{0.6}Fe_{0.3}Cr_{0.1}O_x$ is better than many earth-abundant OER catalysts summarized in Table S2.

The Tafel slopes for both catalysts ($Ni_{0.6}Fe_{0.4}O_x$: 38 ± 3 mV dec^{-1}; $Ni_{0.6}Fe_{0.3}Cr_{0.1}O_x$: 39 ± 2 mV dec^{-1}) are similar, suggesting that they have the same rate limiting step (Fig. S7) [28]. The intrinsic activity of $Ni_{0.6}Fe_{0.4}O_x$ and $Ni_{0.6}Fe_{0.3}Cr_{0.1}O_x$ is evaluated by quantitative determination of a turnover frequency (TOF), which is defined by the number of molecules of oxygen generated by per active site per second (assuming each metal atom is an active site here with the total number of metals determined by ICP-OES). The TOF at 300 mV overpotential in 0.1 M KOH of $Ni_{0.6}Fe_{0.3}Cr_{0.1}O_x$ is $0.046 \pm 0.004\ s^{-1}$, which is 31% higher than that of $Ni_{0.6}Fe_{0.4}O_x$ (0.035 ± 0.007).

3.3. Mechanism analysis and the role of Cr

Limited research has been performed on Cr containing ternary mixed-metal electrocatalysts for OER [18–21]. For instance, Singh and coworkers synthesized a series of spinel-type $NiFe_{2-x}Cr_xO_4$ oxides by the precipitation method, and the best electrocatalytic activity of the oxide was achieved with $x = 0.8–1.0$ [18]. Stahl and coworkers also observed that OER activity was enhanced using annealed Cr-doped Ni–Fe oxides via a fluorescence-based parallel screening method [20]. In neither instance did the studies propose a possible mechanism associated with improved OER activity upon Cr cooperation. In a separate investigation, Lange and coworkers correlated OER activity of annealed $Ni_{1-y-z}Fe_yCr_zO_x$ with electronic structure in a high-throughput study. Results obtained by soft X-ray absorption spectroscopy characterization, suggested that OER activity benefited from an increased ratio of octahedral Fe^{III} to tetrahedral Fe^{III} with the addition of Cr. The thermally prepared oxides they start with would be expected, however, to covert *in situ* to layered hydroxide/oxyhydroxides, at least at the surface where catalysis takes place [3]. As a result of this transformation, there is massive change in the electrochemically accessible surface area (ECSA). To avoid this challenge, in the current investigation we start with an amorphous phase, which could rapidly transform into (oxy)hydroxides during electrochemical activation. The OER activity is discussed along with observed changes in the ECSA in order to investigate whether the observed increase in catalytic activity is intrinsic or due to increasing ECSA. As discussed in detail below, we find that the increased activity is due to increased ECSA due to Cr leaching. This simple mechanism is likely applicable to all of the above studies as the surface-active species in the oxide phases are likely similar to that studies here and the structure of bulk oxide relatively unimportant.

To estimate the ECSA, two methods are typically used: double layer capacitance (C_{DL}) and integration of Ni redox features in voltammetry [29–31]. The ECSA calculated by cyclic voltammetry of scan rate dependence at non-faradaic region is disregarded. Because of the low conductivity ($\sim 10^{-6}\ S\ cm^{-1}$) of uncharged Ni(Fe) (oxy)hydroxides, the measured capacitance is just that of the underlying conductive substrate [29]. We first used AC impedance to measure the C_{DL} for estimating the ECSA (Fig. S8). The equivalent circuit consists of uncompensated solution resistance (R_u) in series with a charge transfer resistance (R_{CT}) and C_{DL} in parallel (Fig. 3a). The C_{DL} is negligible until the potential is close to the $Ni^{2+/3+}$ anodic oxidation peak. After oxidation of the Ni, the catalyst is electrically conductive and C_{DL} can be reliably measured, which is consistent to the previous research [29]. The C_{DL} of $Ni_{0.6}Fe_{0.3}Cr_{0.1}O_x$ was calculated as $13.7 \pm 0.7\ mF\ cm^{-2}$, which is 27% higher than the C_{DL} of $Ni_{0.6}Fe_{0.4}O_x$ ($10.8 \pm 0.8\ mF\ cm^{-2}$).

An alternative method to estimate the ECSA is to calculate the fraction of electrochemically accessible nickel. Due to the overlap between the $Ni^{2+/3+}$ anodic oxidation peak and the OER current for high Fe content Ni–Fe (oxy)hydroxides, the $Ni^{2+/3+}$ reduction peak was integrated. The fraction of electrochemically accessible Ni can be determined from the ratio of the integrated charge in the $Ni^{2+/3+}$ reduction peaks to the total Ni from ICP-OES. The fraction of electrochemically accessible Ni in $Ni_{0.6}Fe_{0.3}Cr_{0.1}O_x$ was calculated to be 0.32 ± 0.02, which is 33% higher than that for $Ni_{0.6}Fe_{0.4}O_x$ 0.24 ± 0.01 (Fig. 3b). These data imply that the ~30% increase in TOF of the Cr containing films can be entirely explained by the ~30% increase in ECSA.

Stability is also of great importance for electrocatalysts [32]. Compared to crystalline catalysts, amorphous catalysts are often less stable, which leads to slow decay over time for some compositions [16,33]. To further assess the catalyst stability and the variation of OER performance, chronopotentiometric measurements were performed at $10\ mA\ cm^{-2}$, without *iR*-compensation, to accelerate the aging process on both activated $Ni_{0.6}Fe_{0.4}O_x$ and $Ni_{0.6}Fe_{0.3}Cr_{0.1}O_x$ on Au/Ti substrate (Fig. 4a). Bubble accumulation on the catalyst surface during these measurements created significant noise. Therefore CVs were collected after each 4 h chronopotentiometry step to determine the OER activity. The overpotential of $Ni_{0.6}Fe_{0.4}O_x$ for water oxidation ($J = 10\ mA\ cm^{-2}$) increased slightly over time: an increase of 10 mV was observed

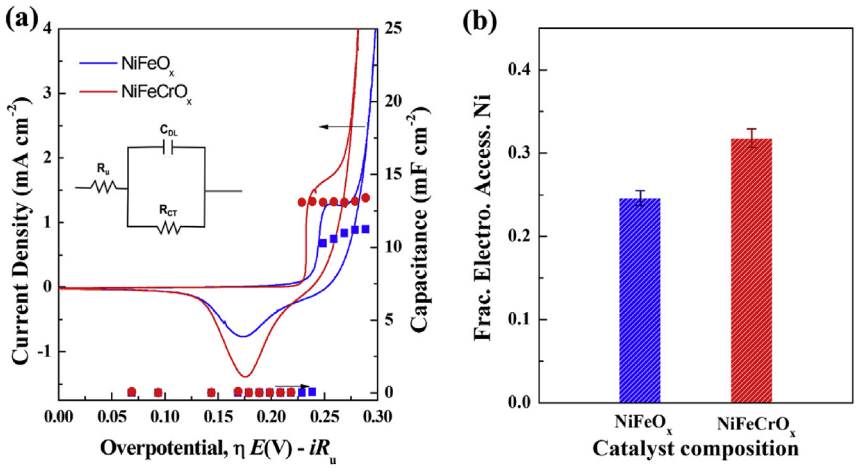

Fig. 3. (a) Voltammetry of $Ni_{0.6}Fe_{0.4}O_x$ and $Ni_{0.6}Fe_{0.3}Cr_{0.1}O_x$ after 100 cycles of CVs and the corresponding double layer capacitance C_{DL} determined by AC impedance as a function of potential. (b) Fraction of electrochemically accessible Ni of $Ni_{0.6}Fe_{0.4}O_x$ and $Ni_{0.6}Fe_{0.3}Cr_{0.1}O_x$ is calculated from the ratio of the integrated charge in the Ni reduction peak relative to the total Ni determined by ICP-OES.

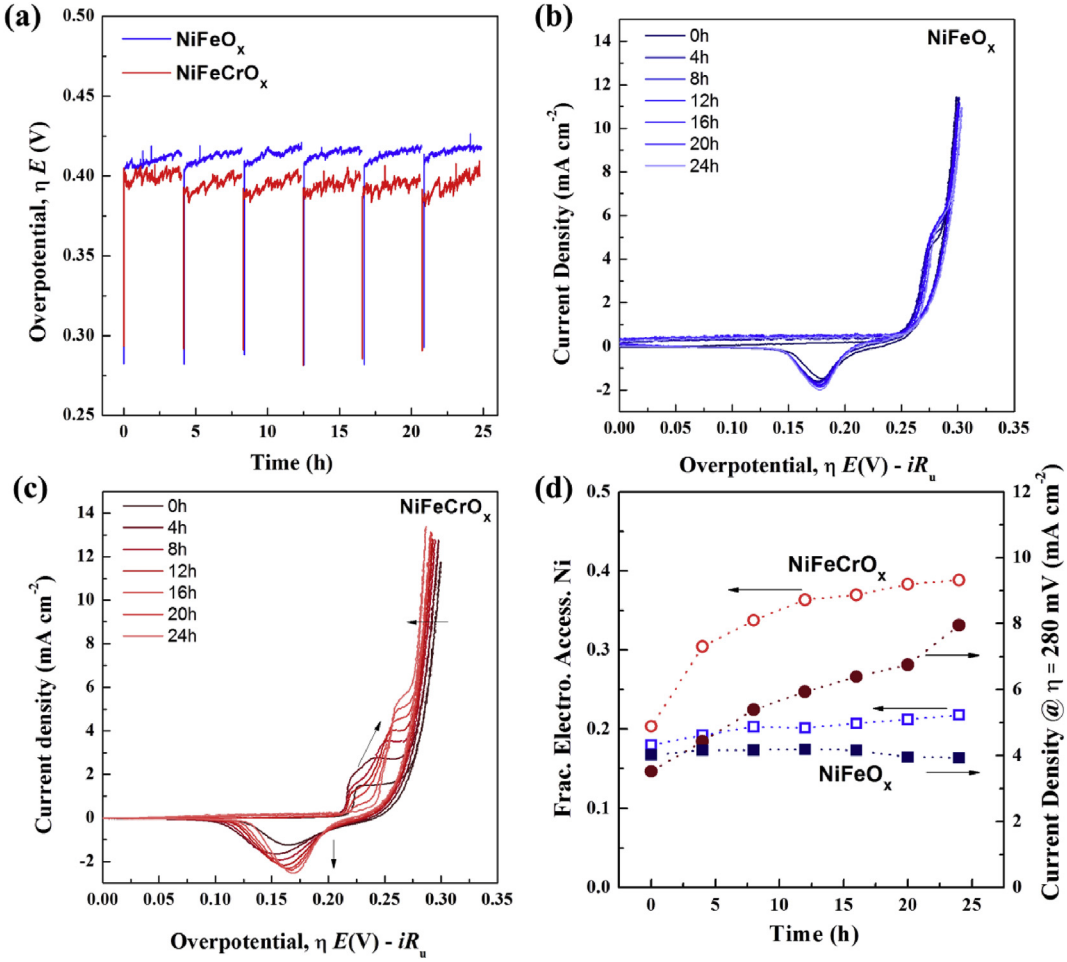

Fig. 4. (a) Chronopotentiometry of $Ni_{0.6}Fe_{0.4}O_x$ and $Ni_{0.6}Fe_{0.3}Cr_{0.1}O_x$ at a constant current density of 10 mA cm^{-2}. Cyclic voltammograms of (c) $Ni_{0.6}Fe_{0.4}O_x$ and (c) $Ni_{0.6}Fe_{0.3}Cr_{0.1}O_x$ were tested at different time points with a scan rate of 10 mV s^{-1}. The CVs are presented after 4 h of polarization (dark to light). (d) Fraction of electrochemically accessible Ni (open symbol) and the current density at 280 mV overpotential (closed symbol) tested at different points in time. The current density was recorded using the data in (b) and (c). All above mentioned electrochemical tests were measured in 0.1 M KOH on Au/Ti substrates.

after 24 h of continuous oxidation reaction (Fig. 4b). In marked contrast, the overpotential for $Ni_{0.6}Fe_{0.3}Cr_{0.1}O_x$ decreased by 15 mV, and the CV curves of $Ni_{0.6}Fe_{0.3}Cr_{0.1}O_x$ show the growth of the Ni oxidation peak as well as a shift to more anodic potentials (Fig. 4c). The Ni reduction peak also shows an obvious growth, while exhibits a complex shift first cathodic then anodic, indicating a more

complicated electronic interaction occurs during the Cr leaching process [34]. The quantitative analysis between the fraction of electrochemically accessible Ni and the current density during time is summarized in Fig. 4d, where the OER activity is proportional to the ECSA. More importantly, $Ni_{0.6}Fe_{0.3}Cr_{0.1}O_x$ became more active even after 24 h stability test. These results imply some changes to structure and/or composition occurred, which in turn further activated the ternary catalyst.

The composition of the films was then determined by ICP-OES (bulk) and XPS (surface) at different time points. The variation of composition of each element determined by ICP-OES is shown in Fig. 5. The initial bulk content of Cr is 14.0% measured by ICP-OES for the as-prepared samples, and a gradual decrease was observed with time. And it decreased to 7.9% after CVs, 5.2% after 4 h stability test, until there is only 2.1% remaining in the film after 24 h. Meanwhile, the bulk ratio of Ni to Fe remains constant. The surface content of Cr was 6.9% measured by XPS for the as-prepared sample. After 24 h stability test the Cr could not be detected. This demonstrates that the Cr leaches during the OER process. A similar phenomenon is also observed by Corrigan for the electrodeposited $Ni_{0.9}Cr_{0.1}O_xH_y$ in which the Cr content decreased from 11.2% for the as-prepared sample to 0.4% after voltammetry experiment, indicating that Cr was leached out in 1 M KOH [35].

Additionally, XPS was used to analyze the changes in composition on the catalyst surface. It should be noted that the XPS discussed here is *ex situ* data, so the oxidation states are unlikely to be representative of the oxidation states during OER. Fig. 6 shows the X-ray photoelectron (XP) spectra of four samples: films as-synthesized and after 24 h test for both $Ni_{0.6}Fe_{0.4}O_x$ and $Ni_{0.6}Fe_{0.3}Cr_{0.1}O_x$ on Au/Ti (Fig. 6a). The representative and distinct changes are highlighted in grey. For both as-deposited samples, Ni is observed by the Ni $2p_{3/2}$ at 855.9 eV (Fig. 6b which is characteristic of both $Ni(OH)_2$ and NiOOH) [36]. The Fe 2p XP spectra are shown in Fig. 6c. The Fe 2p spectra of the four samples show negligible change after the OER test. Because of the similar spectra shapes and binding energy of higher Fe oxides, the specific phase of Fe oxide cannot be confirmed. Fe is likely integrated into the NiOOH structure to form well known Ni(Fe)OOH phases [9,37].

The Cr 2p XP spectra of both as-deposited and after OER testing are shown in Fig. 6d. The peaks with binding energy of ~579.6 eV and 588.9 eV correspond to the oxidized state of Cr for the as-deposited sample according to previous research [38]. After stability tests the Cr peak is no longer visible and it is likely that the amount of Cr present is too low to detect by XPS. Except the Cr 2p spectrum, there is negligible change of Ni and Fe 2p spectra for both of $Ni_{0.6}Fe_{0.4}O_x$ and $Ni_{0.6}Fe_{0.3}Cr_{0.1}O_x$, indicating the high stability of the Ni–Fe based catalyst.

To evaluate the elemental composition as a function of film depth, a series of high-resolution XP spectra were acquired following periods of Ar^+-sputtering (Fig. S9). The distribution of each element is uniform except a little bit lower content (~5%) of Fe for initial sample, which might be attributed to a small amount of Fe leaching: Fe species not incorporated into the NiOOH structure are known to be unstable [15,39]. After 720 s sputtering, the Au of the substrate was observed by the characteristic peak of Au $4f_{7/2}$ at 84.6 eV and Au $4f_{5/2}$ at 88.3 eV, respectively. It is not the pure metallic gold, which may be formed under anodic conditions [40–43]. Compared with the surface analysis, the Ar-sputtered spectra did not change substantially, except for the appearance of Ni^0 and Fe^{2+}. A similar phenomenon was observed for $Ni_{0.6}Fe_{0.4}O_x$ (Fig. S10). Consistent with previous observations of electrochemically activated or electrodeposited Ni hydroxides, the appearance of Ni^0 and Fe^{2+} could be attributed to the reducing nature of the Ar^+ ion environment [44].

Combining the above-mentioned investigation of changes in composition with the OER performance map, it can be inferred that the catalytic capability is sensitive to both composition and surface area. Through XPS and ICP-OES analysis we can tell that the elemental composition changes on the surface during the water oxidation process: Ni and Fe are relatively stable, but Cr is not. This is in agreement with the Pourbaix diagram of Cr, which illustrates that Cr is unstable in strong base electrolyte [45,46]. The apparent increase in ECSA was also observed by Singh in spinel $NiFe_{2-x}Cr_xO_4$ [18]. However, they did not analyze the composition variation as a function of polarization, and did not discuss the role that Cr leaching played in the increasing ECSA.

Besides composition analysis, morphology is also investigated before and after the OER test. The SEM images are shown in Figs. S1c and S1d; both of the $Ni_{0.6}Fe_{0.4}O_x$ and $Ni_{0.6}Fe_{0.3}Cr_{0.1}O_x$ show negligible changes at low magnification after OER stability test for 24 h. Nevertheless the R_{rms} measured from AFM images (Fig. S2) changed significantly, which corresponds to the observed structural rearrangement [3]. The R_{rms} of $Ni_{0.6}Fe_{0.3}Cr_{0.1}O_x$ (1.90 nm) is higher than the $Ni_{0.6}Fe_{0.4}O_x$ (1.22 nm). Leaching of Cr presumably caused the increased surface rough.

These results presented above show that the Cr is leaching during the water oxidation process, which results in the growth of ECSA, as well as more electrochemically accessible active sites. The catalytic performance improved with the decreasing Cr content, demonstrating that Cr itself is unrelated the *intrinsic activity* for Ni–Fe (oxy)hydroxides. Rather it appears that the Cr component serves as a "pore forming" additive, which leads to an acceleration in the number of active sites during its dissolution. Consequently, the OER performance is increased. The electronic interaction

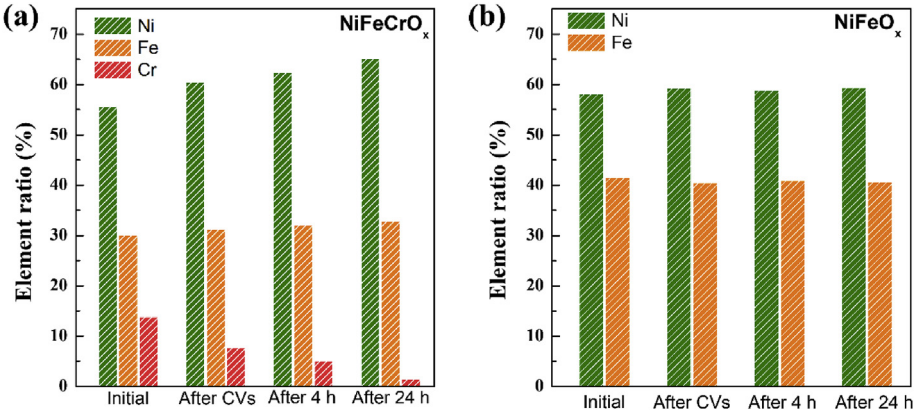

Fig. 5. The element percentage of $Ni_{0.6}Fe_{0.3}Cr_{0.1}O_x$ (a) and $Ni_{0.6}Fe_{0.4}O_x$ (b) at different time points, extracted from Table S1.

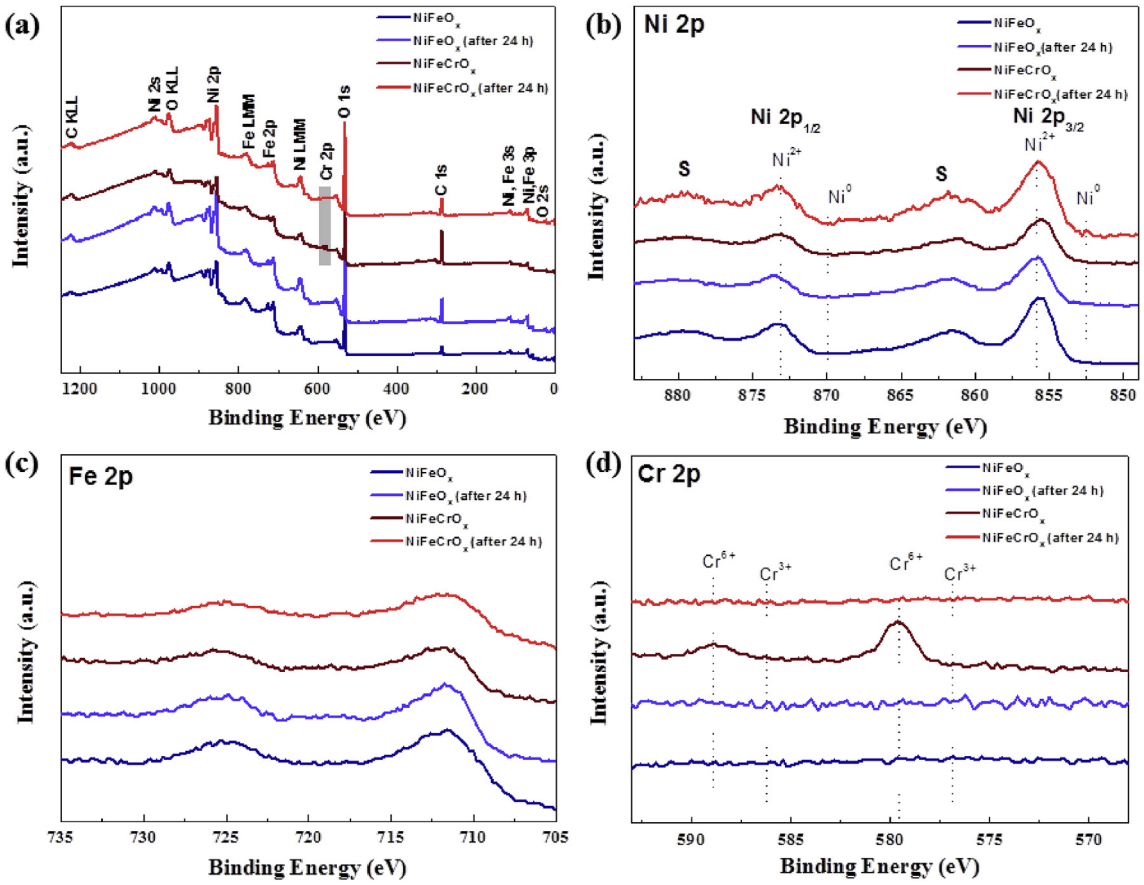

Fig. 6. XP spectra of $Ni_{0.6}Fe_{0.4}O_x$, and $Ni_{0.6}Fe_{0.3}Cr_{0.1}O_x$, as-deposited and after OER stability test, shown are survey (a), Ni 2p (b), Fe 2p (c) and Cr 2p (d) regions.

between Cr and Ni(Fe) could have some detrimental effect on the OER activity based on the voltammetry (Fig. 4c). However, incorporated with the ICP-OES data (Fig. 5a) at different time points, the lower Cr content results in higher OER activity, which confirm that the electronic interaction exists but not corresponding to the promoted OER activity. This demonstration is contrary to the previous articles (ref 18, 19, 20 and 21), which consider the Cr has some interaction of electron structure or the modification of M-O bond strength corresponding to the superior OER activity. The analysis methods used in this study could explain the function of Cr in Ni–Fe oxides/(oxy)hydroxides even other Cr-containing electrocatalysts such as CoCr LDH [47] and $Co_{1-x}Cr_xO_4$ [48], and also could be generalized to other polynary electrocatalysts to investigate the function of theoretically unstable element such as Sr, Ba, W, V, Mo, and Al et al., which have previously been thought to increase the intrinsic activity but as suggested in this investigation, might result in primarily structural and ESCA changes [26,49–52].

The leaching process discovered here has some similarities to the well-known de-alloying strategy: unstable elements are initially alloyed with stable elements, then removed through dissolution to create a nanoporous film [53], skeletal surface [54] or lattice contracted core-shell structure [55], which can be applied to batteries electrodes, current collectors or electrocatalysts.

3.4. Construction of a high-surface-area electrode

The eventual goal for OER catalysts is to have high loaded, high surface area materials that do not lose activity with high mass loading. High catalyst surface areas and loadings can be engineered on porous electrode materials [56]. Carbon cloth (CC) is a low-cost textile with high conductivity, excellent flexibility, and strength, which is commercially available as a support to integrate electrocatalysts for fabrication of these high-surface-area electrodes [57]. Although the disadvantage of CC is that it is unlikely to be stable under practical OER electrolysis conditions long term, the usage of CC here allows for a cheap, high-surface-area template [58]. This method could likely be translated to other high surface area substrates. To confirm the appropriate interfacial bonding and the wettability between the precursor paste and CC substrate, the contact-angle was performed. Fig. S11 shows the aqueous solution contact-angle of CC is 142.5°, and the precursor solution contact-angle is near 0°. That is due to the absence of oxygen-containing functional groups, and the CC shows excellent wettability of the oily precursor solution ($M(Acac)_x$/hexane) [59]. Because CC can absorb much more infrared radiation than FTO, the precursor on CC decomposed faster (1.5 h) than on FTO (2 h) as shown in Fig. S3b.

The morphology of bare CC and the electrocatalyst ($Ni_{0.6}Fe_{0.3}Cr_{0.1}O_x$) anchored CC is as shown in Fig. S12. The loading amount on CC was about 2 mg cm^{-2}. The surface of bare CC was smooth and veined. Comparatively speaking, the CC surface was covered by a continuous, uniform and conformal electrocatalyst “paste”, which turned rougher after coating with electrocatalyst (Figs. S12d–S12f). This results from the superior wettability and excellent interface bonding between precursor and CC substrate. In addition, catalyst/CC electrodes showed improved performance for water oxidation (Figs. S13 and S14). The overpotential of $Ni_{0.6}Fe_{0.3}Cr_{0.1}O_x$ is 251 mV at 10 mA cm^{-2} in 1 M KOH solution, which is lower than the 272 mV required for $Ni_{0.6}Fe_{0.4}O_x$. Their performance is better than many Ni-based oxides/(oxy)hydroxides, phosphate, selenides and even commercial IrO_x [8,60–62].

4. Conclusions

In summary, ternary amorphous electrocatalysts containing Ni, Fe, and Cr were synthesized on FTO and Au/Ti via a simple thermal decomposition method. The performance of ternary electrocatalysts for OER with different compositions was carefully mapped. It was found that the electrocatalyst showed superior water oxidation performance when doped with a small amount of Cr in the binary Ni–Fe oxides/(oxy)hydroxides. The mechanism associated with the increased activity was determined to results from increasing ECSA and thus the number of active sites.

We also reported a $Ni_{0.6}Fe_{0.3}Cr_{0.1}O_x$ catalyst with a low overpotential of 232 ± 2 mV at a current density of 1 mA cm^{-2} as well as a small Tafel slope of 39 ± 2 mV dec^{-1} in 0.1 M KOH solution. The outstanding electrocatalytic performance of $Ni_{0.6}Fe_{0.3}Cr_{0.1}O_x$ was attributed to the high intrinsic activity of Ni–Fe (oxy)hydroxides and high porosity obtained through Cr leaching and the initial amorphous structure. And contrary to previous findings, we propose that the chromium begins to leach immediately upon electrochemical testing and, the chromium is almost completely depleted after a 24 h stability test. Importantly, along with the decreased content of chromium, the catalyst activity is further promoted. Although the chromium itself may not be responsible for the improvement, its dissolution results in an ideal type of pore and/or active sites.

The precursor was also coated on carbon cloth to fabricate high-surface-area electrodes. The $Ni_{0.6}Fe_{0.3}Cr_{0.1}O_x$/CC showed the overpotential as low as 251 mV to achieve a current density of 10 mA cm^{-2} in 1 M KOH. The analysis method presented here could provide a model for the continued fundamental study of amorphous multi-metal electrocatalysts. The mechanistic insight derived from dopant behavior suggests new ideas and methods for the construction of porous, disordered and high-efficiency catalysts for OER and other heterogeneous catalysis areas.

Acknowledgement

We gratefully acknowledge the financial support by Natural Science Foundation of China (No.51572046, 51503035), Science and Technology Commission of Shanghai Municipality (13JC1400200), the Shanghai Natural Science Foundation (15ZR1401200), the Program for Professor of Special Appointment (Eastern Scholar) at Shanghai Institutions of Higher Learning, Program of Shanghai Academic Research Leader (16XD1400100), the Program of Introducing Talents of Discipline to Universities (No.111-2-04), the National Science Foundation East Asia and Pacific Summer Institute Fellowship (OISE1613514), and the Fundamental Research Funds for the Central Universities (2232014A3-06). D.X. thanks the Special Excellent PhD International Visiting Program, the Fundamental Research Funds for the Central Universities (16D310603) and Advanced Materials Characterization in Oregon (CAMCOR). Research performed at the University of Oregon was supported by the US National Science Foundation, grant number CHE-1566348.

Appendix A. Supplementary data

Supplementary data related to this article can be found at https://doi.org/10.1016/j.electacta.2018.01.143.

References

[1] M.G. Walter, E.L. Warren, J.R. McKone, S.W. Boettcher, Q. Mi, E.A. Santori, N.S. Lewis, Solar water splitting cells, Chem. Rev. 110 (2010) 6446–6473.
[2] V.R. Stamenkovic, D. Strmcnik, P.P. Lopes, N.M. Markovic, Energy and fuels from electrochemical interfaces, Nat. Mater. 16 (2017) 57–69.
[3] L. Trotochaud, J.K. Ranney, K.N. Williams, S.W. Boettcher, Solution-cast metal oxide thin film electrocatalysts for oxygen evolution, J. Am. Chem. Soc. 134 (2012) 17253–17261.
[4] M.S. Burke, M.G. Kast, L. Trotochaud, A.M. Smith, S.W. Boettcher, Cobalt-iron (oxy)hydroxide oxygen evolution electrocatalysts: the role of structure and composition on activity, stability, and mechanism, J. Am. Chem. Soc. 137 (2015) 3638–3648.
[5] J. Suntivich, K.J. May, H.A. Gasteiger, J.B. Goodenough, Y. Shao-Horn, A perovskite oxide optimized for oxygen evolution catalysis from molecular orbital principles, Science 334 (2011) 1383–1385.
[6] M.S. Burke, L.J. Enman, A.S. Batchellor, S. Zou, S.W. Boettcher, Oxygen evolution reaction electrocatalysis on transition metal oxides and (Oxy)hydroxides: activity trends and design principles, Chem. Mater. 27 (2015) 7549–7558.
[7] C.C. McCrory, S. Jung, J.C. Peters, T.F. Jaramillo, Benchmarking heterogeneous electrocatalysts for the oxygen evolution reaction, J. Am. Chem. Soc. 135 (2013) 16977–16987.
[8] T. Zhan, X. Liu, S. Lu, W. Hou, Nitrogen doped NiFe layered double hydroxide/reduced graphene oxide mesoporous nanosphere as an effective bifunctional electrocatalyst for oxygen reduction and evolution reactions, Appl. Catal. B Environ. 205 (2017) 551–558.
[9] L. Trotochaud, S.L. Young, J.K. Ranney, S.W. Boettcher, Nickel-iron oxyhydroxide oxygen-evolution electrocatalysts: the role of intentional and incidental iron incorporation, J. Am. Chem. Soc. 136 (2014) 6744–6753.
[10] R. Subbaraman, D. Tripkovic, K.-C. Chang, D. Strmcnik, A.P. Paulikas, P. Hirunsit, M. Chan, J. Greeley, V. Stamenkovic, N.M. Markovic, Trends in activity for the water electrolyser reactions on 3d M (Ni, Co, Fe, Mn) hydr (oxy) oxide catalysts, Nat. Mater. 11 (2012) 550.
[11] I.C. Man, H.-Y. Su, F. Calle-Vallejo, H.A. Hansen, J.I. Martínez, N.G. Inoglu, J. Kitchin, T.F. Jaramillo, J.K. Nørskov, J. Rossmeisl, Universality in oxygen evolution electrocatalysis on oxide surfaces, ChemCatChem 3 (2011) 1159–1165.
[12] D.A. Corrigan, The catalysis of the oxygen evolution reaction by iron impurities in thin film nickel oxide electrodes, J. Electrochem. Soc. 134 (1987) 377–384.
[13] N. Li, D.K. Bediako, R.G. Hadt, D. Hayes, T.J. Kempa, F. von Cube, D.C. Bell, L.X. Chen, D.G. Nocera, Influence of iron doping on tetravalent nickel content in catalytic oxygen evolving films, Proc. Natl. Acad. Sci. U. S. A. 114 (2017) 1486–1491.
[14] M. Görlin, J. Ferreira de Araujo, H. Schmies, D. Bernsmeier, S.r. Dresp, M. Gliech, Z. Jusys, P. Chernev, R. Kraehnert, H. Dau, Tracking catalyst redox states and reaction dynamics in Ni–Fe oxyhydroxide oxygen evolution reaction electrocatalysts: the role of catalyst support and electrolyte pH, J. Am. Chem. Soc. 139 (2017) 2070–2082.
[15] D. Friebel, M.W. Louie, M. Bajdich, K.E. Sanwald, Y. Cai, A.M. Wise, M.-J. Cheng, D. Sokaras, T.-C. Weng, R. Alonso-Mori, Identification of highly active Fe sites in (Ni, Fe) OOH for electrocatalytic water splitting, J. Am. Chem. Soc. 137 (2015) 1305–1313.
[16] R.D. Smith, M.S. Prevot, R.D. Fagan, Z. Zhang, P.A. Sedach, M.K. Siu, S. Trudel, C.P. Berlinguette, Photochemical route for accessing amorphous metal oxide materials for water oxidation catalysis, Science 340 (2013) 60–63.
[17] C. Zhang, R.D. Fagan, R.D.L. Smith, S.A. Moore, C.P. Berlinguette, S. Trudel, Mapping the performance of amorphous ternary metal oxide water oxidation catalysts containing aluminium, J. Mater. Chem. 3 (2015) 756–761.
[18] R.N. Singh, J.P. Singh, B. Lal, M.J.K. Thomas, S. Bera, New $NiFe_{2-x}Cr_xO_4$ spinel films for O_2 evolution in alkaline solutions, Electrochim. Acta 51 (2006) 5515–5523.
[19] C. Schwanke, H.S. Stein, L. Xi, K. Sliozberg, W. Schuhmann, A. Ludwig, K.M. Lange, Correlating oxygen evolution catalysts activity and electronic Structure by a high-throughput investigation of $Ni_{1-y-z}Fe_yCr_zO_x$, Sci. Rep. 7 (2017) 44192.
[20] J.B. Gerken, S.E. Shaner, R.C. Massé, N.J. Porubsky, S.S. Stahl, A survey of diverse earth abundant oxygen evolution electrocatalysts showing enhanced activity from Ni-Fe oxides containing a third metal, Energy Environ. Sci. 7 (2014) 2376–2382.
[21] O. Diaz-Morales, I. Ledezma-Yanez, M.T. Koper, F. Calle-Vallejo, Guidelines for the Rational Design of Ni-based Double Hydroxide Electrocatalysts for the Oxygen Evolution Reaction, 2015.
[22] A. Indra, P.W. Menezes, N.R. Sahraie, A. Bergmann, C. Das, M. Tallarida, D. Schmeißer, P. Strasser, M. Driess, Unification of catalytic water oxidation and oxygen reduction reactions: amorphous beat crystalline cobalt iron oxides, J. Am. Chem. Soc. 136 (2014) 17530–17536.
[23] H.Y. Wang, S.F. Hung, H.Y. Chen, T.S. Chan, H.M. Chen, B. Liu, Operando identification of geometrical-site-dependent water oxidation activity of spinel Co3O4, J. Am. Chem. Soc. 138 (2016) 36–39.
[24] C.W. Tung, Y.Y. Hsu, Y.P. Shen, Y. Zheng, T.S. Chan, H.S. Sheu, Y.C. Cheng, H.M. Chen, Reversible adapting layer produces robust single-crystal electrocatalyst for oxygen evolution, Nat. Commun. 6 (2015) 8106.
[25] A. Bergmann, E. Martinez-Moreno, D. Teschner, P. Chernev, M. Gliech, J.F. de Araujo, T. Reier, H. Dau, P. Strasser, Reversible amorphization and the catalytically active state of crystalline Co_3O_4 during oxygen evolution, Nat. Commun. 6 (2015) 8625.
[26] K.J. May, C.E. Carlton, K.A. Stoerzinger, M. Risch, J. Suntivich, Y.-L. Lee, A. Grimaud, Y. Shao-Horn, Influence of oxygen evolution during water oxidation on the surface of perovskite oxide catalysts, J. Phys. Chem. Lett. 3 (2012) 3264–3270.
[27] D.A. Salvatore, K.E. Dettelbach, J.R. Hudkins, C.P. Berlinguette, Near-

infrared–driven decomposition of metal precursors yields amorphous electrocatalytic films, Sci. Adv. 1 (2015), e1400215.
[28] D.K. Bediako, C. Costentin, E.C. Jones, D.G. Nocera, J.-M. Saveant, Proton–electron transport and transfer in electrocatalytic films. Application to a cobalt-based O_2-Evolution catalyst, J. Am. Chem. Soc. 135 (2013) 10492–10502.
[29] A.S. Batchellor, S.W. Boettcher, Pulse-electrodeposited Ni–Fe (Oxy)hydroxide oxygen evolution electrocatalysts with high geometric and intrinsic activities at large mass loadings, ACS Catal. 5 (2015) 6680–6689.
[30] G.C. da Silva, N. Perini, E.A. Ticianelli, Effect of temperature on the activities and stabilities of hydrothermally prepared IrOx nanocatalyst layers for the oxygen evolution reaction, Appl. Catal. B Environ. 218 (2017) 287–297.
[31] T. Audichon, B. Guenot, S. Baranton, M. Cretin, C. Lamy, C. Coutanceau, Preparation and characterization of supported RuxIr(1-x)O2 nano-oxides using a modified polyol synthesis assisted by microwave activation for energy storage applications, Appl. Catal. B Environ. 200 (2017) 493–502.
[32] M.S. Burke, M.G. Kast, L. Trotochaud, A.M. Smith, S.W. Boettcher, Cobalt–iron (oxy) hydroxide oxygen evolution electrocatalysts: the role of structure and composition on activity, stability, and mechanism, J. Am. Chem. Soc. 137 (2015) 3638–3648.
[33] R.D. Smith, M.S. Prévot, R.D. Fagan, S. Trudel, C.P. Berlinguette, Water oxidation catalysis: electrocatalytic response to metal stoichiometry in amorphous metal oxide films containing iron, cobalt, and nickel, J. Am. Chem. Soc. 135 (2013) 11580–11586.
[34] L.J. Enman, M.S. Burke, A.S. Batchellor, S.W. Boettcher, Effects of intentionally incorporated metal cations on the oxygen evolution electrocatalytic activity of nickel (Oxy)hydroxide in alkaline media, ACS Catal. 6 (2016) 2416–2423.
[35] D.A. Corrigan, R.M. Bendert, Effect of coprecipitated metal ions on the electrochemistry of nickel hydroxide thin films: cyclic voltammetry in 1M KOH, J. Electrochem. Soc. 136 (1989) 723–728.
[36] M.C. Biesinger, B.P. Payne, L.W. Lau, A. Gerson, R.S.C. Smart, X-ray photoelectron spectroscopic chemical state quantification of mixed nickel metal, oxide and hydroxide systems, Surf. Interface Anal. 41 (2009) 324–332.
[37] M.W. Louie, A.T. Bell, An investigation of thin-film Ni-Fe oxide catalysts for the electrochemical evolution of oxygen, J. Am. Chem. Soc. 135 (2013) 12329–12337.
[38] I. Milošev, H.-H. Strehblow, B. Navinšek, XPS in the study of high-temperature oxidation of CrN and TiN hard coatings, Surf. Coating. Technol. 74 (1995) 897–902.
[39] F.D. Speck, K.E. Dettelbach, R.S. Sherbo, D.A. Salvatore, A. Huang, C.P. Berlinguette, On the electrolytic stability of iron-nickel oxides, Chem 2 (2017) 590–597.
[40] S. Zou, M.S. Burke, M.G. Kast, J. Fan, N. Danilovic, S.W. Boettcher, Fe (Oxy) hydroxide oxygen evolution reaction electrocatalysis: intrinsic activity and the roles of electrical conductivity, substrate, and dissolution, Chem. Mater. 27 (2015) 8011–8020.
[41] A. Visco, X-ray photoelectron spectroscopy of Au/Fe_2O_3 catalysts, Phys. Chem. Chem. Phys. 1 (1999) 2869–2873.
[42] K. Juodkazis, J. Juodkazyt, V. Jasulaitien, A. Lukinskas, B. Šebeka, XPS studies on the gold oxide surface layer formation, Electrochem. Commun. 2 (2000) 503–507.
[43] S. Minicò, S. Scirè, C. Crisafulli, S. Galvagno, Influence of catalyst pretreatments on volatile organic compounds oxidation over gold/iron oxide, Appl. Catal. B Environ. 34 (2001) 277–285.
[44] F.A. Laskowski, M.R. Nellist, R. Venkatkarthick, S.W. Boettcher, Junction behavior of n-Si photoanodes protected by thin Ni elucidated from dual working electrode photoelectrochemistry, Energy Environ. Sci. 10 (2017) 570–579.
[45] B. Beverskog, I. Puigdomenech, Revised Pourbaix diagrams for chromium at 25–300 C, Corrosion Sci. 39 (1997) 43–57.
[46] B. Beverskog, I. Puigdomenech, Pourbaix diagrams for the ternary system of iron-chromium-nickel, Corrosion 55 (1999) 1077–1087.
[47] C. Dong, X. Yuan, X. Wang, X. Liu, W. Dong, R. Wang, Y. Duan, F. Huang, Rational design of cobalt–chromium layered double hydroxide as a highly efficient electrocatalyst for water oxidation, J. Mater. Chem. 4 (2016) 11292–11298.
[48] C.-C. Lin, C.C. McCrory, Effect of chromium doping on electrochemical water oxidation activity by Co3–x Cr x O4 spinel catalysts, ACS Catal. 7 (2016) 443–451.
[49] J. Suntivich, K.J. May, H.A. Gasteiger, J.B. Goodenough, Y. Shao-Horn, A perovskite oxide optimized for oxygen evolution catalysis from molecular orbital principles, Science 334 (2011) 1383–1385.
[50] J.Y. Chen, J.T. Miller, J.B. Gerken, S.S. Stahl, Inverse spinel $NiFeAlO_4$ as a highly active oxygen evolution electrocatalyst: promotion of activity by a redox-inert metal ion, Energy Environ. Sci. 7 (2014) 1382–1386.
[51] X. Shang, K.-L. Yan, S.-S. Lu, B. Dong, W.-K. Gao, J.-Q. Chi, Z.-Z. Liu, Y.-M. Chai, C.-G. Liu, Controlling electrodeposited ultrathin amorphous Fe hydroxides film on V-doped nickel sulfide nanowires as efficient electrocatalyst for water oxidation, J. Power Sources 363 (2017) 44–53.
[52] K.-L. Yan, J.-F. Qin, Z.-Z. Liu, B. Dong, J.-Q. Chi, W.-K. Gao, J.-H. Lin, Y.-M. Chai, C.-G. Liu, Organic-inorganic hybrids-directed ternary NiFeMoS anemone-like nanorods with scaly surface supported on nickel foam for efficient overall water splitting, Chem. Eng. J. 334 (2018) 922–931.
[53] C. Hitz, A. Lasia, Experimental study and modeling of impedance of the her on porous Ni electrodes, J. Electroanal. Chem. 500 (2001) 213–222.
[54] X. Lang, A. Hirata, T. Fujita, M. Chen, Nanoporous metal/oxide hybrid electrodes for electrochemical supercapacitors, Nat. Nanotechnol. 6 (2011) 232–236.
[55] P. Strasser, S. Koh, T. Anniyev, J. Greeley, K. More, C. Yu, Z. Liu, S. Kaya, D. Nordlund, H. Ogasawara, Lattice-strain control of the activity in dealloyed core–shell fuel cell catalysts, Nat. Chem. 2 (2010) 454–460.
[56] Y. Leng, G. Chen, A.J. Mendoza, T.B. Tighe, M.A. Hickner, C.Y. Wang, Solid-state water electrolysis with an alkaline membrane, J. Am. Chem. Soc. 134 (2012) 9054–9057.
[57] Z. Pu, Q. Liu, A.M. Asiri, X. Sun, Tungsten phosphide nanorod arrays directly grown on carbon cloth: a highly efficient and stable hydrogen evolution cathode at all pH values, ACS Appl. Mater. Interfaces 6 (2014) 21874–21879.
[58] S.-E. Jang, H. Kim, Effect of water electrolysis catalysts on carbon corrosion in polymer electrolyte membrane fuel cells, J. Am. Chem. Soc. 132 (2010) 14700–14701.
[59] E. Gauthier, T. Hellstern, I.G. Kevrekidis, J. Benziger, Drop detachment and motion on fuel cell electrode materials, ACS Appl. Mater. Interfaces 4 (2012) 761–771.
[60] A. Sivanantham, S. Shanmugam, Nickel selenide supported on nickel foam as an efficient and durable non-precious electrocatalyst for the alkaline water electrolysis, Appl. Catal. B Environ. 203 (2017) 485–493.
[61] S.H. Ahn, B.-S. Lee, I. Choi, S.J. Yoo, H.-J. Kim, E. Cho, D. Henkensmeier, S.W. Nam, S.-K. Kim, J.H. Jang, Development of a membrane electrode assembly for alkaline water electrolysis by direct electrodeposition of nickel on carbon papers, Appl. Catal. B Environ. 154 (2014) 197–205.
[62] J. Chang, Q. Lv, G. Li, J. Ge, C. Liu, W. Xing, Core-shell structured Ni 12 P 5/Ni 3 (PO 4) 2 hollow spheres as difunctional and efficient electrocatalysts for overall water electrolysis, Appl. Catal. B Environ. 204 (2017) 486–496.